Available online at www.sciencedirect.com
SCIENCE DIRECT
International Journal of Heat and Mass Transfer 49 (2006) 1603–1618
International Journal of HEAT and MASS TRANSFER
www.elsevier.com/locate/ijhmt

Steady evaporating flow in rectangular microchannels

R.H. Nilson [a,*], S.W. Tchikanda [a], S.K. Griffiths [a], M.J. Martinez [b]

[a] Fluid and Thermal Sciences Department, Sandia National Laboratories, Livermore, CA 94551-0969, United States
[b] Multiphase Transport Processes Department, Sandia National Laboratories, Albuquerque, NM 87185-0834, United States

Received 16 March 2005; received in revised form 20 August 2005
Available online 10 January 2006

Abstract

Analytical and numerical solutions are presented for steady evaporating flow in open microchannels having a rectangular cross section and a uniform depth. The flow, driven by the axial gradient of capillary pressure, generally consists of an entry region where the meniscus is attached to the top corners of the channel followed by a jump-like transition to a corner-flow region in which the meniscus progressively recedes into the bottom corners of the channel. Illustrative numerical solutions are used to guide the derivation of an easily applied analytical approximation for the maximum sustainable heat flux or capillary limit.

Keywords: Heat pipes; Microfluidics; Capillary flow; Evaporative cooling; Microgrooves

1. Introduction

Heat pipes and capillary pumped loops utilize the capillary suction of a wick material to draw liquid into the evaporation region, eliminating the need for active pumping of the coolant. Traditional wicks are made of a porous material such as a sintered metal, a felt metal, or a layered screen [1]. More recently, a number of microfabrication technologies have been used to produce engineered wick structures that provide a better balance between the opposing requirements of increased capillary suction (small pores) and reduced frictional flow resistance (large pores). Electrical discharge machining (EDM) of metals and chemical etching of silicon have been used to create microgrooves having triangular, trapezoidal, sinusoidal, and nearly rectangular cross sections [2–4].

Triangular grooves have received by far the most attention in the literature [4–12]. The axial flow along the channel is typically analyzed using a one-dimensional model containing a friction coefficient relating the mean fluid speed to the viscous shear stresses and gravitational forces that oppose the driving capillary pressure gradient. The required friction coefficients are described by analytical or tabular functions of the channel geometry and the fluid/solid contact angle [12–16]. These relationships are pre-determined by solving the two-dimensional Navier–Stokes equations that apply in the cross sectional plane of the channel.

In addition to modeling the bulk axial flow, some analyses have included detailed modeling of the thin film region immediately adjacent to the fluid/solid contact where most of the evaporation occurs [5,9–11]. This nanoscale region has microscale implications because the apparent contact angle is dependent upon the local evaporation rate adjacent to the meniscus contact line [9–11,17–19]. Indeed, for the case of perfectly wetting systems Morris [18,19] has derived, and verified by comparison with experimental data, an easily applied formula for the apparent contact angle as a function of the local evaporation rate and material properties. Similarly, in partially wetting systems, local evaporation will produce an apparent contact angle that differs from the static or minimum contact angle determined by fluid/solid surface energies.

Boundary conditions at the channel inlet also influence the contact angle between fluid and solid. To our

* Corresponding author.
E-mail address: rhnilso@sandia.gov (R.H. Nilson).

0017-9310/$ - see front matter © 2005 Elsevier Ltd. All rights reserved.
doi:10.1016/j.ijheatmasstransfer.2005.11.002

Nomenclature

A	channel aspect ratio, D/W
A_{cc}	cross sectional area of channel
A_ℓ	area occupied by liquid
$C_{1,2}$	constants in Eqs. (18) and (19)
D	channel depth
G^*	normalized gravitational acceleration
g_x	gravitational acceleration along channel
h	liquid depth at channel side wall
h_c	liquid depth at channel center
H_{fg}	latent heat of vaporization
L	channel length
p	fluid pressure
p_c	capillary pressure
p^*	normalized fluid pressure
q''	heat flux applied to channel bottom
Q^*	normalized heat flux
R	radius of meniscus curvature
R_0	characteristic curvature in Eq. (6)
s	liquid saturation or volume fraction
t	time
u	mean liquid speed
W	channel width
W_b	base width including wall thickness

Greek symbols

α	fluid/solid contact angle
β	friction factor defined by Eq. (3)
Δ	difference operator
Δp_0	scaling pressure in Eq. (6)
$\Delta\xi_{cor}$	normalized extent of corner flow
λ	W/h_c, in Appendix A
Λ	$W/(h-h_c)$, in Appendix A
μ	liquid viscosity
θ	angle defined in Eq. (A2)
Θ	parameter defined in Eq. (34)
ρ	liquid mass density
σ	surface tension
τ	dimensionless time
Ω	parameter defined in Eq. (37)
ξ	normalized axial position, x/L

Subscripts

cor	corner flow
D	dryout location
G	match point (gravity flows)
M	match point (corner flow)
min	minimum value
max	maximum value
ℓ	liquid phase
0	channel inlet or reference
v	vapor phase

Superscript

*	normalized quantity

knowledge, only one previous study [6], addressing capillary flow in triangular grooves, has acknowledged that the channel is often liquid-full at its inlet and that an *accommodation* region or *meniscus deformation* region generally exists wherein the meniscus remains attached to the upper corners of the channel as it adjusts from its inlet configuration to the smaller values associated with the minimum (static) contact angle adjusted for local evaporation. The resulting deformation and elongation of the meniscus gradually reduces the contact angle, causing an axial decrease in the radius of curvature, as depicted schematically in Fig. 1 for a channel of rectangular cross section. The result of this accommodation or meniscus deformation process is to produce an axial gradient of the capillary pressure that may substantially increase fluid flow rates and sustainable heat fluxes. Depending on the relative extent of the accommodation region, the maximum sustainable heat flux may be increased by more than an order of magnitude, compared to that attainable for a constant contact angle.

The focus of prior work on triangular grooves may be largely motivated by ease of prototype fabrication and because the triangular shape provides a monotonic decrease in meniscus radius and capillary pressure as the meniscus

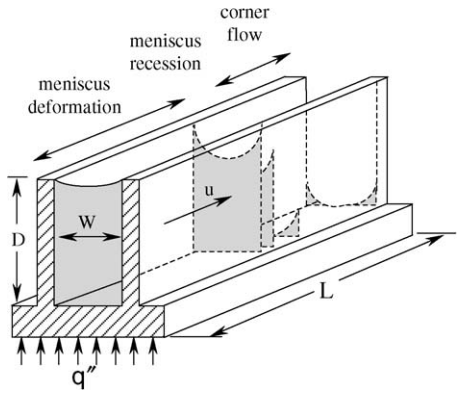

Fig. 1. Schematic of steady evaporating flow along rectangular microchannel. Axial variation of liquid volume fraction creates capillary pressure gradient that drives the axial flow.

recedes into the wedge shaped channel. Although this ensures a continuous axial gradient of capillary pressure, the triangular shape provides only half the cross sectional area of a rectangular channel and the viscous friction is greater, reducing the axial flow rate. In addition, deep triangular cross sections cannot be readily produced using litho-

graphic processes that have been so successful in mass production of semiconductor devices. In contrast, a large multiplicity of rectangular channels having widths down to a few microns and depths ranging up to a millimeter or more can be fabricated using the LIGA process based on electrodeposition of metals into lithographically patterned molds [20,21]. Thus, the focus of the present paper on rectangular channels is partly driven by new manufacturing technologies, though there are certainly prior examples of rectangular microchannels produced by micromachining, saw cutting, and electrical discharge machining.

The present paper addresses steady evaporating flow in microchannels of rectangular cross section. As in most previous analyses of microchannel flows, we restrict our modeling to the bulk axial flow and utilize pre-determined friction coefficients to account for viscous flow resistance. However, unlike previous analyses, our solutions demonstrate the existence of a flow structure having a meniscus deformation region where the meniscus is attached to the top corners of the channel followed by a jump-like transition to a corner-flow region in which the meniscus progressively recedes into the bottom corners. These features of the flow are illustrated by representative numerical results for a range of channel aspect ratios, normalized gravitational forces, and fluid/solid contact angles. In addition, analytical solutions are used to describe the limiting cases of large and small aspect ratios. Finally, the dryout heat flux or "capillary limit" is presented for a broad range of geometric parameters and operating conditions.

Since our primary goal is to illustrate fundamental features of the axial flow structure, we will assume that the heat flux to the base of the channel is simply uniform and we will treat the minimum contact angle as a known and constant quantity that may depend on the applied heat flux. In reality, axial variations of the local heat flux, surface temperature, and the contact angle are determined by the heat source geometry, heat conduction in the channel walls and substrate, and the local contact line physics, coupled with the axial capillary flow that we focus upon in the present paper. However, the flow equations presented here can be readily integrated for a variable heat flux and it is possible to integrate these other aspects of the coupled physics into the capillary flow model described below.

2. Flow geometry and capillary pressure

Fig. 2 illustrates the cross sectional geometry of a rectangular microchannel containing a liquid separated from the adjacent gas phase by a curved meniscus. The capillary pressure, p_c, representing the pressure difference across the liquid/vapor interface, $p_v - p_\ell$, is given by the Young–Laplace equation

$$p_c = p_v - p_\ell = \frac{\sigma}{R} \tag{1}$$

in which σ is the surface tension and R is the radius of meniscus curvature in the cross sectional plane. Since the channel length, L, is generally much greater than the channel width, W, the local capillary pressure is controlled mainly by the transverse curvature of the meniscus. Moreover, since the Bond number $Bo = \rho g W^2/\sigma$ is usually small in channels of submillimeter width, the radius of curvature may be taken as constant at any axial cross section. This approximation is made with the understanding that a change in curvature may occur as the circular meniscus merges into a submicron thin film that often covers portions of the channel wall [2,3]. Although the presence of such a thin film obscures the meaning of a contact angle, this angle can still be defined in a macroscopic sense as the angle between the side wall and a circular meniscus extended to meet the wall. An apparent contact point or contact line can be defined in the same manner. Since the axial flow is only sensitive to the macroscopic radius, r, the thin film physics are conveniently incorporated through their influence on the apparent contact angle, α, relating the channel width to the macroscopic radius of curvature, $R = W/(2\cos\alpha)$. For simplicity, we will assume here that the external vapor pressure, p_v, is uniform so that pressure gradients in the liquid result only from changes in the capillary pressure. However, it is understood than in many devices there will be an aiding or opposing pressure gradient associated with the parallel flow of evaporated vapor.

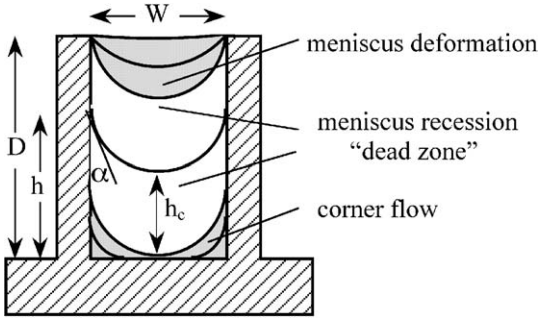

Fig. 2. Liquid configuration within rectangular channel. Meniscus curvature and capillary pressure vary with liquid volume fraction within shaded zones but not in dead zone.

Three different regimes of meniscus geometry are identified in Fig. 2. All three of these may apply over different axial regions of the same channel, as in transient wetting processes or in steady evaporating flows where the fluid depth decreases along the channel, as in Fig. 1. Here, we use the term *regime* to describe the alternative wetting geometries depicted in Fig. 2. In contrast, the term *region* refers to the axial domain or axial extent of a particular flow regime. When the meniscus is attached to the top corners of the channel, the small but finite corner radius or the singular character of a sharp corner permit the contact angle to vary freely so long as it remains greater than the minimum contact angle that applies when the meniscus leaves the corner and moves downward onto the planar wall. In this meniscus deformation or accommodation regime [6], shown shaded at the top of Fig. 2, the liquid pressure decreases as the meniscus bows downward into

the channel, decreasing the radius of curvature and the contact angle.

After reaching the minimum contact angle, further reductions in liquid content cause the meniscus to detach from the top corners and retreat toward the channel bottom. The central portion of this regime, shown unshaded in Fig. 2, has been referred to as the *dead zone* [3]. Within this regime, the contact angle has a constant value determined by surface energy considerations and the local evaporation rate [17–19]. Thus, in a channel of uniform width, the radius of curvature remains constant for all meniscus positions between the fully bowed meniscus attached to the top corners and a position near the bottom where the center of the meniscus contacts the channel floor. Over this central range of meniscus positions there is no variation in the capillary pressure and hence no pressure gradient to drive a flow of liquid along a dead zone of finite length. As we shall see, the axial extent of the dead zone is minimized by the formation of a very steep saturation gradient, approaching a discontinuous saturation jump when the axial curvature of the liquid/vapor interface is neglected, as it is in the present mathematical model.

When the meniscus reaches the channel bottom, it splits into a pair of separate menisci that are each attached to the bottom and to one of the side walls. Within this regime, a pair of identical *corner flows* are driven by the reduction in liquid pressure that occurs as the triangular zone of liquid recedes into the corner. The transition from a single meniscus that spans the channel into separate corner menisci is continuous only for a minimum contact angle of 0° since this is the only case where the meniscus has a contact angle of 0° at the bottom center of the channel just before and just after the meniscus touches the bottom. Thus, the transition generally involves an abrupt change in saturation but the capillary pressure must be continuous.

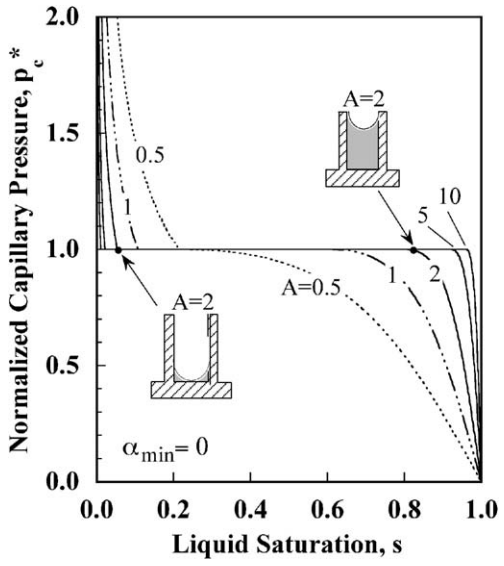

Fig. 3. Variation of normalized capillary pressure with fractional saturation (liquid volume fraction) for a minimum contact angle of 0°. Plateau corresponds to dead zone. $A = D/H$.

Fig. 3 shows the variation of the normalized capillary pressure, $p_c^* = p_c/(2\sigma/W)$, with the fluid saturation, s, representing the area fraction or volume fraction of the channel containing liquid. Results are presented for several values of the aspect ratio, $A = D/W$. All three regimes noted earlier in Fig. 2 are readily apparent in Fig. 3. When s is small, the liquid resides only within the bottom corners of the channel. In this corner-flow regime, the radius of curvature is proportional to the wetted height of the side wall; $R \sim h$. Further since $s \sim h^2$ it follows that $p_c = \sigma/R \sim 1/s^{1/2}$ so that the capillary pressure based on continuum concepts becomes infinite as s approaches 0. Although this limiting behavior will ultimately be influenced by molecular scale physics [17], these nanoscale effects do not alter the microscopic process of interest here. At intermediate values of s, there is usually a plateau of uniform capillary pressure corresponding to the dead zone illustrated earlier in Fig. 2. All states to the right of the plateau correspond to the meniscus deformation regime in which the circular meniscus is attached to the top corners of the channel. Here, the capillary pressure again decreases monotonically as the bowing of the meniscus decreases with increasing saturation. Finally, as s approaches unity, the capillary pressure goes to 0, corresponding to a liquid-full channel having a flat interface and, hence, an infinite radius of curvature.

The width of the dead-zone plateau increases with increasing aspect ratio (depth/width), exceeding 90% of the overall saturation range for $A > 4$. Further, the plateau in Fig. 3 vanishes for an aspect ratio of 0.5, leaving a continuous transition between the corner-flow regime and the meniscus deformation regime. This continuous transition is a special case that occurs only for a minimum contact angle of 0° and only for an aspect ratio of 0.5. In this case alone, the meniscus comes into contact with the channel floor just as it reaches its fully bowed form, so there is no dead-zone plateau and the angle of the meniscus at the contact point is the same both before and after contact.

For contact angles greater than 0, the free surface always undergoes an abrupt, nearly discontinuous, transition when the spanning meniscus splits into separate corner menisci. This is because the apparent contact angle at the bottom changes abruptly from 0°, as required by symmetry just before contact, to the nonzero value that applies after contact. Since the pressure and the radius of curvature must be continuous across the saturation jump, the fluid saturation on the corner-flow side of jump must decrease with increasing values of the contact angle, as illustrated in Fig. 4. This behavior can be understood by considering the limiting case of a corner meniscus with a 45° contact angle. Here, the radius of curvature is infinite and the capillary pressure is zero no matter how small the saturation, even though the circular meniscus attached to the side walls prior to the jump had a finite capillary pressure. A corner meniscus having a somewhat smaller contact angle, say 40°, can produce a significant capillary pressure, but only for a very small saturation of $s < 0.01$ in Fig. 4. Note that

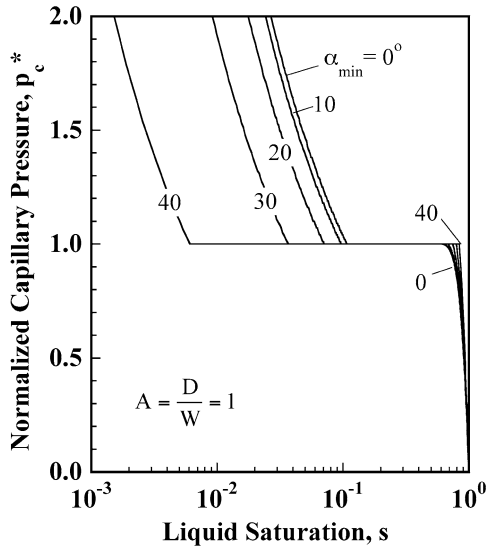

Fig. 4. Comparison of capillary pressure curves for minimum contact angles ranging from 0° to 40°.

contact angles exceeding 45° would require a change in free surface curvature from concave to convex, preventing the formation of corner flows ahead of the primary flow that spans the full channel width.

Capillary pressure curves like those shown in Figs. 3 and 4 are constructed by geometric analysis of the flow configurations shown in Fig. 2. A summary of the needed geometric relations is given in Appendix A. The resulting capillary pressure curves serve as constitutive information to be used in solving the one-dimensional form of the axial transport equations, as explained below.

3. Governing equations

The mass conservation equation describing transient evaporating flow along the rectangular microchannel of Fig. 1 may be written in the following one-dimensional form:

$$\frac{\partial}{\partial t}(\rho A_{cc} s) + \frac{\partial}{\partial x}(\rho u A_{cc} s) = -\frac{q'' W_b}{H_{fg}} \tag{2}$$

Here, t is the time, x is the axial position, ρ is the liquid density, u is the mean axial speed, $A_{cc} = DW$ is the cross sectional area of a channel of uniform width W and depth D, s is the liquid saturation describing the volume fraction of the channel containing liquid, and H_{fg} is the heat of evaporation. It is assumed here that all of the heat flux q'' applied to the channel bottom is consumed by local fluid evaporation, requiring that temperature variations within the system be moderate ($c_p \Delta T \ll H_{fg}$). This criterion is usually well satisfied. The heat flux, here assumed uniform, is applied to a base of width W_b, somewhat greater then the corresponding channel width, W, owing to the presence of walls between neighboring channels. Usually, $W_b = W + B$ where B is the thickness of the channel side wall.

The axial liquid speed, u, is determined by the balance between the viscous friction force, $\mu u \beta / W^2$, the gravity force acting along the channel, ρg_x, and the gradient of the liquid pressure, p_ℓ,

$$u = -\frac{W^2}{\beta \mu}\left(\frac{\partial p_\ell}{\partial x} + \rho g_x\right) \tag{3}$$

The viscosity μ is presumed uniform and the sign of the gravitational term implies that a positive gravity force opposes the pressure driven flow. The parameter β appearing in the denominator is a friction coefficient that is simply the reciprocal of the normalized mean fluid speed, U^*, defined in [16] $\beta = 1/U^*$. Appendix A provides a brief description of the analytical expression used to compute β from local values of the contact angle, fluid depth and channel geometry. This expression is based upon blending of analytical results that apply in asymptotic limits of fluid depth and contact angle, with the blending parameters chosen to obtain best agreement with detailed numerical solutions [16].

Combination of Eqs. (2) and (3) yields a single partial differential equation describing axial variations of the normalized liquid pressure, p_ℓ^*, and saturation, s

$$\frac{\partial s}{\partial \tau} - \frac{\partial}{\partial \xi}\left(\frac{s}{\beta}\left(\frac{\partial p_\ell^*}{\partial \xi} + G^*\right)\right) = -Q^* \tag{4}$$

The non-dimensional variables appearing here have been scaled in the following manner:

$$\xi = \frac{x}{L} \quad p_\ell^* = \frac{p_\ell - p_v}{\Delta p_0} \quad \tau = \frac{t W^2 \Delta p_0}{\mu L^2} \tag{5}$$

Here, L is the channel length and p_v is the vapor pressure that is assumed to be uniform above the channel. Δp_0 is the capillary pressure of a spanning circular meniscus in a channel of width W when the wetting angle is at its minimum value, α_{min}. The corresponding radius of curvature is $R_0 = W/(2\cos\alpha_{min})$ and hence

$$\Delta p_0 = \frac{\sigma}{R_0} = 2\cos\alpha_{min}\frac{\sigma}{W} \tag{6}$$

The two dimensionless parameters in Eq. (4) are the normalized heat flux Q^* and the normalized gravitational force, G^*

$$Q^* \equiv \frac{q''}{D\rho H_{fg}}\left(\frac{\mu}{\Delta p_0}\right)\frac{W_b L^2}{W^3} \quad G^* = \frac{\rho g_x L}{\Delta p_0} \tag{7}$$

The two unknown functions, p_ℓ^* and s, appearing in Eq. (4) are generally related by capillary pressure curves like those shown in Figs. 3 and 4. Further, since we are assuming that there is no axial gradient of the gas pressure, we may take p_v as the zero or datum level so that the normalized capillary pressure, p_c^*, is simply the negative of the normalized liquid pressure, p_ℓ^*.

$$p_c^*(s) \equiv \frac{p_v - p_\ell}{\Delta p_0} = -p_\ell^*(s) \tag{8}$$

Thus, given that the capillary pressure is a known function of s, we can rewrite Eq. (4) as follows in terms of s alone.

$$\frac{\partial s}{\partial \tau}+\frac{\partial}{\partial \xi}\left(\frac{s}{\beta}\left(\frac{\mathrm{d}p_c^*}{\mathrm{d}s}\frac{\partial s}{\partial \xi}-G^*\right)\right)=-Q^* \tag{9}$$

Here $\mathrm{d}p_c^*/\mathrm{d}s$ is the slope of the capillary pressure curve and is readily obtained by analytical or numerical differentiation of functions like those shown in Figs. 3 and 4.

Although we are mainly interested in steady solutions to the governing equations, these solutions are computed by a time-marching finite-volume solution procedure. To ensure diagonal dominance, we utilize a one-sided "upwind" difference approach dependent upon the signs of the quantities shown below in square brackets.

$$\frac{\partial s}{\partial \tau}+\frac{\partial}{\partial \xi}\left(\left[\frac{s}{\beta}\frac{\mathrm{d}p_c^*}{\mathrm{d}s}\right]\frac{\partial s}{\partial \xi}\right)-\frac{\partial}{\partial \xi}\left(s\left[\frac{G^*}{\beta}\right]\right)=-Q^* \tag{10}$$

The square bracketed quantities are evaluated at cell faces and are iteratively updated several times at each time step to obtain a fully implicit scheme. The number of grid points along the flow is chosen to be relatively large, typically 500 or more, mainly to obtain fine resolution of saturation jumps without introducing any specialized front tracking or localized grid refinement procedures. Roughly 1000 time steps are typically required to reach a steady state.

During the course of the solution, it is necessary to obtain numerous values of the capillary pressure gradient, $\mathrm{d}p_c^*/\mathrm{d}s$, and the friction coefficient, β, as a function of the instantaneous saturation. This is done using the relationships outlined in Appendix A where the fractional saturation is written as an explicit function of fluid depth, contact angle, and channel dimensions. This relationship can be readily inverted by a procedure which first identifies the appropriate wetting regime (meniscus deformation, dead zone, corner flow) based on precomputed values of the saturations that define the boundaries of these regimes. Once the regime has been identified, the liquid depth can be determined by inverting single-parameter geometric relations appropriate to that regime. Alternatively, the capillary pressure curves can be precomputed and stored in tabular form suitable for subsequent interpolation.

The boundary condition at the inlet is a prescribed saturation, usually $s(0,\tau)=1$. At the far end of the channel the axial saturation gradient is set to zero to prevent flow through the end wall. The initial saturation profile, $s(\xi,0)$, is taken as uniform at either 0 or 1; either choice yields the same steady solution. In many of the illustrative calculations the flow does not penetrate all the way to the end of the channel, as often observed in experimental studies. In these examples, the wetted length of the channel gives a good indication of the influence of various parameters. However, the absence of evaporative cooling at the dry end of the channel would often be unacceptable in applications such as cooling of microelectronics. Thus, to compute the maximum sustainable heat flux, $Q^*_{\max}$ we sometimes perform iterative adjustments of Q^* to determine the largest value of Q^* for which the fluid penetrates all the way to the channel end at $\xi=1$.

4. Continuous flow structures

Computed steady profiles of fluid saturation, normalized liquid velocity, and normalized liquid pressure are shown in Fig. 5 for a minimum contact angle of 0° and for a normalized gravitational force of $G^*=0$. Here and hereafter, the normalized velocity is defined as

$$u^*=\frac{u}{u_0}=\frac{uL\mu}{W^2\Delta p_0} \tag{11}$$

The aspect ratio in Fig. 5 is $A=0.5$, corresponding to the capillary pressure curve in Fig. 3 having no plateau. Note in Fig. 5a that the fluid saturation at the channel inlet is unity, indicating that the meniscus is flat across the top of the channel corresponding to an infinite radius of curvature and hence a vanishing capillary pressure at the inlet, $p_0^*\equiv p_\ell^*(0)=0$.

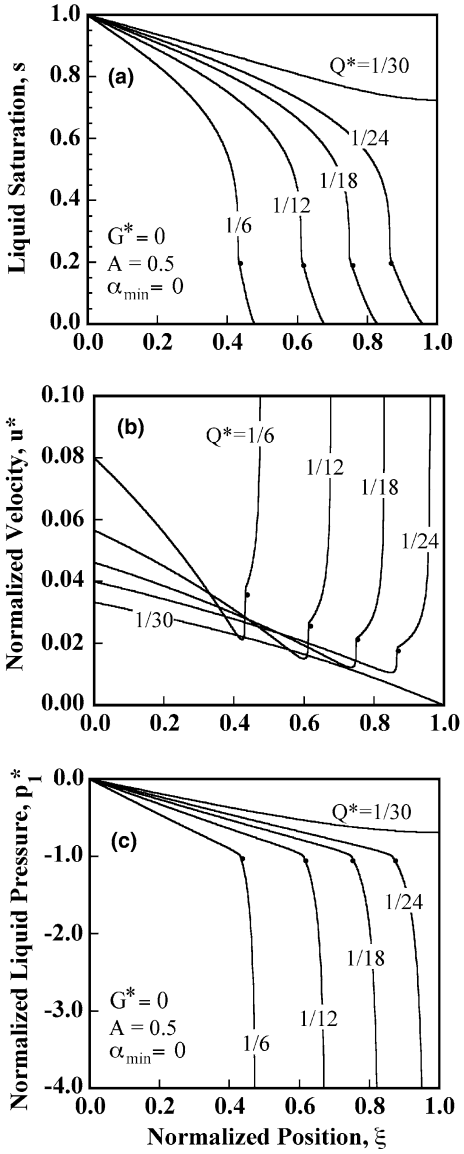

Fig. 5. Profiles of (a) fractional saturation, (b) velocity, and (c) pressure along channel for various applied heat fluxes, Q^*, with $G^*=0$, $A=0.5$, $\alpha_{\min}=0°$, $p_0^*=0$. Saturation profile is always continuous for $A=0.5$.

With increasing heat flux, Q^*, the steady liquid content within the channel is progressively reduced. For $Q^* = 1/30$, the liquid saturation or volume fraction at the far end of the channel is moderately depressed to a level of about $s = 0.7$, increasing the downward bowing of the meniscus. This reduces the radius of meniscus curvature and reduces the pressure in the liquid phase, thereby creating the pressure gradient that draws liquid down the channel. However, for $Q^* = 1/24$, the liquid can no longer penetrate to the end of the channel. Still larger values of Q^* cause further reductions in the liquid penetration distance along the channel.

The saturation profiles in Fig. 5a for $Q^* = 1/24$, 1/18, 1/12, and 1/6 all have the same basic structure. In the entry region of the flow, the meniscus is attached to the top corners of the channel, and the reduction in liquid saturation is accommodated by increased bowing of the meniscus. The saturation gradient becomes infinite at the approach to a sharp kink in the saturation profile. At this point the meniscus is just touching the floor of the channel and, as seen earlier in Fig. 3, dp_c^*/ds approaches 0, and this requires that $ds/d\xi$ approach infinity in order to maintain the forward flow. However, immediately to the right of the kink in Fig. 5, $ds/d\xi$ remains finite, in keeping with the finite value of dp_c^*/ds on the left hand side of the kink in Fig. 3.

The velocity profiles in Fig. 5b are generally smooth and nearly linearly within the meniscus deformation region where the meniscus remains attached to the top corners of the channel. For the smallest value of Q^*, this deformation region extends over the full length of the flow. However, when the flow fails to reach the end of the channel, the velocity appears to approach infinity at the dryout point where the saturation approaches 0; this will be verified later analytically. In addition, there is a sharp increase in velocity as the flow approaches the transition point between the meniscus deformation region and the corner-flow region. This steep rise in velocity is needed to offset the steep reduction in saturation explained in the preceding paragraph. These two trends toward infinite but opposing gradients in saturation and velocity conspire to produce a linearly decreasing variation of the product, us, as required by Eq. (2). Although the velocity gradient approaches infinity on the left of the transition point, the velocity itself remains finite and must be continuous across the transition, since the mass flux and the saturation are both clearly continuous.

The pressure profiles in Fig. 5c are unremarkable except for the very steep pressure gradient at the dryout locations of the flows that fail to reach the end of the channel. At these points the pressure gradient becomes infinite and the computed liquid pressure tends toward negative infinity. In reality, these trends are modified by additional thin film physics that become important at very low saturations but are, for simplicity, excluded from our model. However, the solutions presented here should be largely insensitive to these details except in the immediate vicinity of the dryout location. Since the neglected physics would presumably mitigate the infinite pressure gradient predicted by the current model, we would anticipate a slight shortening of the corner-flow portion of the flow structure.

5. Saturation jumps

Saturation jumps may form in channels having sufficiently large aspect ratios, as illustrated by the results presented in Fig. 6. Here, the minimum contact angle and the normalized gravitational force are still 0, as previously in Fig. 5. However, the normalized heat flux is now held fixed at $Q^* = 1/6$ while the aspect ratio A is varied from 0.5 to 10. Thus, the result shown for $A = 0.5$ is identical to that shown previously in Fig. 5 for $Q^* = 1/6$. For larger aspect ratios the liquid penetration length along the channel is

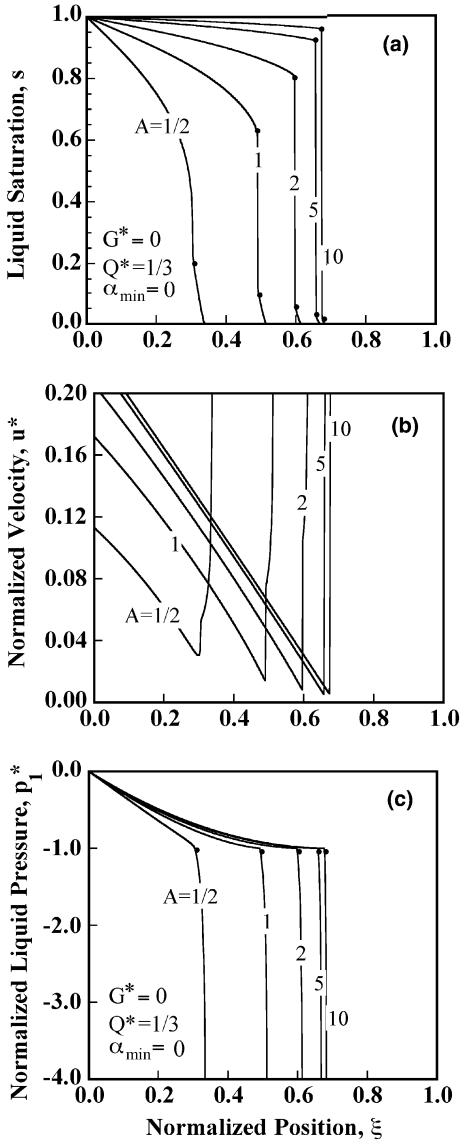

Fig. 6. Profiles of (a) fractional saturation, (b) velocity, and (c) pressure along channel for various aspect ratios, A, with $Q^* = 1/6$, $G^* = 0$, $\alpha_{min} = 0°$, $p_0^* = 0$. Saturation jump is present for $A > 0.5$.

greater. This increase in penetration length holds true, even though the scaling of the normalized heat flux, Q^*, already includes a linear dependence on the channel depth D. Accordingly, one can apply a heat flux that is proportional to the channel depth and still expect to see a longer penetration for a channel of high aspect ratio, all channels having the same width. This stronger than linear dependence of penetration length on A results from the combined effects of two factors that both increase the fluid flow rate, increased cross sectional area and reduced friction. The reduction in friction is realized because an increase in fluid depth reduces the importance of the frictional forces on the channel bottom.

The magnitudes of the saturation jumps in Fig. 6 are identical to the breadths of the plateaus seen earlier in the capillary pressure curves of Fig. 3. Thus, the discontinuity in saturation corresponds to a jump across the plateau region previously identified as the *dead zone* in Fig. 2. The necessity of this jump is readily demonstrated by axially integrating the steady form of Eq. (4), assuming an axially uniform Q^*, to obtain

$$\frac{s}{\beta}\left[-\frac{\mathrm{d}p_\ell^*}{\mathrm{d}\xi}-G^*\right]=\frac{s}{\beta}\left[\frac{\mathrm{d}p_c^*}{\mathrm{d}s}\frac{\mathrm{d}s}{\mathrm{d}\xi}-G^*\right]=+Q^*(\xi_D-\xi) \qquad (12)$$

This expression incorporates the boundary condition that there be no flow beyond the point $\xi=\xi_D$ representing either the dryout location or the end of the channel. Since the right hand side of Eq. (12) is everywhere positive, it follows that the quantity in square brackets must also be everywhere positive. This requirement is easily satisfied over portions of the saturation profile where $\mathrm{d}p_c^*/\mathrm{d}s<0$ and $\mathrm{d}s/\mathrm{d}\xi<0$. However, since $\mathrm{d}p_c^*/\mathrm{d}s=0$ over the entire breadth of the dead zone, it follows that $s(\xi)$ cannot be continuous over any potion of this range when $G^*\geqslant 0$. However, when $G^*<0$ the gravitational force aids the flow along the channel, and Eq. (12) can be satisfied by the following smooth nearly linear decrease of saturation within the dead zone where $\mathrm{d}p_c^*/\mathrm{d}s=0$.

$$s=-\frac{Q^*\beta}{G^*}(\xi_D-\xi) \quad \text{or} \quad \frac{\mathrm{d}s}{\mathrm{d}\xi}\approx\frac{Q^*\beta}{G^*}<0 \qquad (13)$$

In keeping with the discontinuous saturation profiles of Fig. 6, the slope of the saturation profile becomes progressively steeper with decreasing G^*, approaching a jump as G^* approaches 0.

Fig. 7 illustrates the influence of G^* on the axial saturation profile for an aspect ratio of $A=2$, an applied heat flux of $Q^*=1/3$, and a contact angle of 0°. With increasing G^*, the penetration depth is reduced, as expected, since a positive value of G^* indicates a gravitational force that opposes the capillary driven flow. In addition it is seen that for $G^*<0$ the magnitude of the saturation jump decreases as G^* becomes increasing negative. Consistent with Eq. (13), a larger portion of the dead zone is now traversed by a smooth decline in saturation. As also predicted by Eq. (13), the slope of the saturation profile within the dead zone becomes flatter as the magnitude of G^* increases.

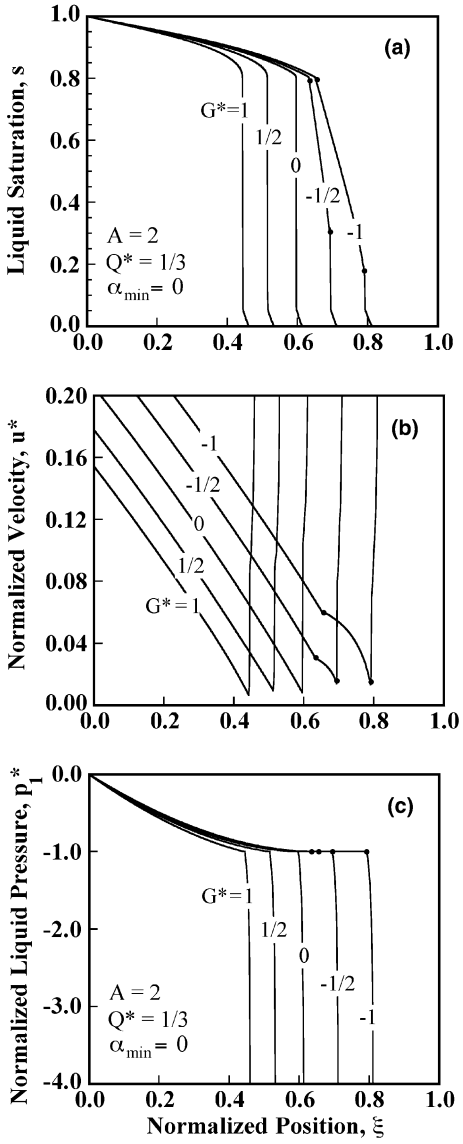

Fig. 7. Profiles of (a) fractional saturation, (b) velocity, and (c) pressure along channel for various normalized gravitational forces, G^*, with $A=2$, $Q^*=1/3$, $\alpha_{\min}=0°$, $p_0^*=0$. Saturation jump is diminished when gravity aids flow.

Also, for any given fixed value of G^*, the slope of the saturation profile becomes slightly steeper with decreasing saturation because the friction coefficient, β, increases with decreasing fluid depth.

Abrupt transitions like the saturation jumps described in the preceding section will always be smeared over a transition region of finite thickness by some secondary physical process. The saturation discontinuities of the present mathematical solutions can be removed by locally accounting for the axial component of meniscus curvature. To estimate the axial extent, δ, of the transition region we first note that the axial radius of meniscus curvature, R_{axial}, is related as follows to the depth profile of the liquid

$$\frac{1}{R_{\text{axial}}}=\frac{\mathrm{d}^2h_c}{\mathrm{d}x^2}\left(1+(\mathrm{d}h_c/\mathrm{d}x)^2\right)^{-3/2}\approx\frac{D}{\delta^2} \qquad (14)$$

where h_c is the local height of the meniscus at the channel center and D is the channel depth. Within the transition region the flow is driven by the axial gradient of this longitudinal component of the capillary pressure.

$$\frac{dp_c}{dx} \approx \frac{d}{dx}\left(\frac{\sigma}{R_{axial}}\right) \approx \frac{\sigma D}{\delta^3} \tag{15}$$

Outside the transition region the flow is driven mainly by the axial gradient of the capillary pressure resulting from the transverse meniscus curvature.

$$\frac{dp_c}{dx} \approx \frac{d}{dx}\left(\frac{\sigma}{R_0}\right) \approx \frac{\sigma w}{2L} \tag{16}$$

Finally, since the flow speed in the transition zone must usually be comparable to that outside, the two pressure gradients noted above must be comparable in magnitude. Equating the above pressure gradients in Eqs. (15) and (16) yields the following estimate for the relative extent of the transition region,

$$\frac{\delta}{L} \approx \left(\frac{wD}{2L^2}\right)^{1/3} \tag{17}$$

Thus, the transition zone is relatively short when D and W are both small compared to L. For example, a typical channel having a width of 0.1 mm, a depth of 0.3 mm, and a length of 2 cm will have a transition zone that is about 3% of the overall channel length. For aspect ratios $A > 1$, the transition zone will be narrower than this because the fluid speed and required capillary pressure gradient just upstream of the saturation jump are generally much smaller than the inlet speed, as apparent in Fig. 6.

Problems like the present one having embedded or boundary-layer regions where higher order derivatives become important have often been successfully attacked using a singular perturbation approach that involves asymptotic matching of inner and outer solutions [22]. In general, discontinuities of the outer solution are locally smoothed over the inner length scale, here δ, without substantially altering the global character of the outer solution, here represented by solutions containing saturation jumps.

6. Analytical solution for corner flows

The preceding numerical results have demonstrated that the overall flow structure generally consists of two distinct regions, the meniscus deformation region and corner-flow region, separated by a saturation jump (for $G^* \geqslant 0$) and/or a linear gradient (for $G^* < 0$) that spans the dead zone of the capillary pressure curve. However, when the aspect ratio is very large, the corner flows are of little significance since the fluid depth in the corners is small compared to the overall channel depth. Conversely, when the channel aspect ratio is relatively small and the inlet meniscus is deeply bowed, only the corner flows are important. Within each of these flow regions, the governing equations can be solved analytically, providing added insights as well as a check on the preceding numerical results.

When the channel aspect ratio is sufficiently small, the meniscus is in contact with the channel floor over most, if not all, of the channel length. Under these conditions liquid resides only within the two corner regions where the side walls meet the channel floor. The fluid geometry within these corners is determined solely by the minimum contact angle and by a single transverse length dimension, here taken as the wetted height of the wall, h in Fig. 2. Note that, for corner flows, the wetted length measured across the channel bottom is equal to the wetted height, since the contact angle is the same on the bottom and side walls. As the flow proceeds along the channel, the local fluid volume is gradually reduced by evaporation causing a reduction in h and a proportional reduction in the radius of curvature.

A differential equation for the axial variation of the wetted height, h, is now derived by rewriting the expressions for saturation, pressure, and velocity in terms of h. First, the cross sectional area occupied by the liquid is simply a constant times the square of h,

$$A_\ell = C_1(\alpha_{min})h^2 = 2\left(1 - \frac{\pi}{4}\right)h^2 \quad \text{for } \alpha_{min} = 0 \tag{18}$$

Here, the second equality applies to the special case of $\alpha_{min} = 0$; a general expression for C_1 is given by Eq. (A3) of Appendix A. Recalling that the full cross sectional area is DW, the fractional saturation is given by $s = A_\ell/DW = C_1h^2/DW$. Further, since the radius of curvature is directly proportional to h, as given by $R = h\cos(\pi/4)/\sin(\pi/4 - \alpha_{min})$, we can write Eq. (1) as

$$p_\ell = -C_2(\alpha_{min})\frac{\sigma}{h} = -\frac{\sin(\pi/4 - \alpha_{min})}{\cos(\pi/4)}\frac{\sigma}{h} \tag{19}$$

with the implication that the liquid pressure gradient can be expressed as the gradient of h. Eq. (3) still relates the pressure gradient to the fluid speed except that the frictional length scale W is replaced by h. In addition, the value of the friction coefficient becomes a function of α alone, and so remains constant along the length of the flow. This function, $\beta(\alpha)$, has been evaluated by Ransohoff and Radke [14]; a value of $\beta = 93.93$ applies for a wetting angle of 0. Substitution of these results into Eq. (1) yields the following differential equation for $h^* = h/W$.

$$\frac{d}{d\xi}\left(h^{*2}\frac{dh^*}{d\xi} + h^{*4}G^*\frac{W}{R_0C_2}\right) = Q^*\frac{D}{R_0}\frac{\beta}{C_1C_2} \equiv \widehat{Q}^* \tag{20}$$

For the case of a horizontal flow with $G^* = 0$, Eq. (20) can be integrated analytically subject to a no-flow boundary condition at $\xi = 1$ to obtain

$$\left(\frac{h^*}{h_0^*}\right)^3 = 1 + 3\frac{\widehat{Q}^*}{h_0^{*3}}\left(\frac{\xi^2}{2} - \xi\right) \tag{21}$$

The maximum sustainable heat flux corresponds to a value of $\widehat{Q}^*_{max} = 2h_0^{*3}/3$ for which h^* approaches 0 at the end of

the channel where $\xi = 1$. Under this incipient dryout condition, the primary dependent variables can written as follows:

$$h^* = h_0^*(1-\xi)^{2/3} = \frac{1}{2}(1-\xi)^{2/3} \tag{22}$$

$$s = C_1 \frac{W}{D} h^{*2} = \left(1 - \frac{\pi}{4}\right)(1-\xi)^{4/3} \tag{23}$$

$$p_\ell^* = -C_2 \frac{R_0}{W}\frac{1}{h^*} = -(1-\xi)^{-2/3} \tag{24}$$

$$u^* = \frac{C_2}{\beta}\frac{R_0}{W}\frac{2}{3}h_0^*(1-\xi)^{-1/3} = \frac{1}{6\beta}(1-\xi)^{-1/3} \tag{25}$$

$$Q^*_{\max,\mathrm{cor}} = \widehat{Q}^*_{\max}\frac{C_1C_2R_0}{D\beta} = \frac{2}{3}h_0^{*3}\frac{C_1C_2R_0}{D\beta} = 3.8\times 10^{-4} \tag{26}$$

Here, the furthest right member of each equation corresponds to the particular case where the minimum contact angle is 0 and the inlet meniscus is attached to the top corners of the channel; hence $h_0 = D = R_0 = W/2$, $h_0^* = 1/2$, $\beta = 94$, $C_1 = 2(1-\pi/4) = 0.429$, $C_2 = 1$.

Fig. 8 shows a comparison of the analytical results given by Eqs. (22)–(26) with numerical calculations (symbols) performed by the method described earlier. The agreement is very good even in the neighborhood of the singularity at the end of the channel where the saturation approaches 0. Here, the velocity and the pressure tend toward the opposite extremes of infinity and negative infinity, respectively. Any such singularity can generally be traced to the neglect or simplification of physical processes that become important in the immediate neighborhood of the singularity. Here we have neglected the disjoining pressure, important in very thin films, and we have simplified the three-dimensional structure of the meniscus at the leading edge of the flow. However, since these phenomena should only be important within one or two channel widths of the leading edge, they should not substantially alter the overall flow structure or the sustainable heat fluxes.

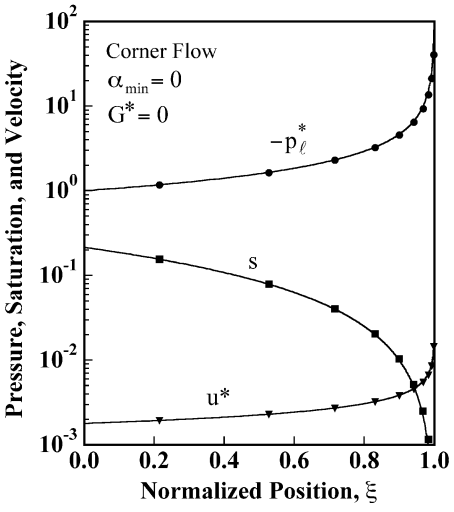

Fig. 8. Comparison of numerical calculations (symbols) with exact analytical solution (solid lines) for flow in the bottom corners of the channel. $G^* = 0$, $A = H/W = 0.5$, $\alpha_{\min} = 0°$, $Q^* = 3.8\times 10^{-4}$, $p_0^* = -1$.

The flow structure illustrated in Fig. 8 should always apply at the leading edge of a steady evaporating flow where the saturation approaches 0, regardless of the upstream flow structure. Furthermore, the gravitation forces neglected in Fig. 8 should have little influence on the leading edge since viscous and pressure forces both become very large as $s \to 0$. Thus, it is not surprising that the same structure is consistently observed at the leading edge of all of the more complex flows illustrated in Figs. 5–7. Indeed, the leading portion of the flow should look identical to that shown in Fig. 8, except that the overall length of the leading structure is shortened from unity in Fig. 8 to a smaller length, $\Delta\xi_{\mathrm{cor}}$,

$$\frac{\Delta\xi_{\mathrm{cor}}}{1} = \left(\frac{Q^*_{\max,\mathrm{cor}}}{Q^*}\right)^{1/2} \tag{27}$$

where $Q^*_{\max,\mathrm{cor}}$ is given by Eq. (26). The square root dependence results from the observation that the square of the fluid penetration length is inversely proportional to the applied heat flux, as apparent in the scaling of Q^* defined by Eq. (7a). As an example, for an aspect ratio of $A = 0.5$ and a normalized heat flux of $Q^* = 1/24$, $\Delta\xi_{\mathrm{cor}} = (24\times\ 3.8\times 10^{-4})^{1/2} \approx 0.1$, in good agreement with the length of the precursor corner flow for $Q^* = 1/24$ in Fig. 5. Similarly, for $A = 2$ and $Q^* = 1/3$, $\Delta\xi_{\mathrm{cor}} = (3\times 3.8\times 10^{-4}/4)^{1/2} \approx 0.02$ in reasonable agreement with the precursor corner flows observed for all G^* in Fig. 7. The factor of 1/4 in the preceding calculation of $\Delta\xi_{\mathrm{cor}}$ accounts for the ratio $R_0/D = 1/4$ (for $A = 2$) appearing in Eq. (26).

Although we cannot analytically integrate Eq. (20) for nonzero G^*, we can roughly estimate the ratio of maximum heat fluxes with and without gravity by forming the following ratio of the bracketed terms on the left side of Eq. (20).

$$\Gamma \approx \frac{Q^*_{\max,\mathrm{w/grav}}}{Q^*_{\max,\mathrm{wo/grav}}} \approx \frac{h^{*2}\dfrac{\mathrm{d}h^*}{\mathrm{d}\xi} + h^{*4}G^*\dfrac{W}{R_0C_2}}{h^{*2}\dfrac{\mathrm{d}h^*}{\mathrm{d}\xi}} \tag{28}$$

Making the substitutions $h^* \approx \bar{h}^* \approx h_0^*/2$ and $\mathrm{d}h^*/\mathrm{d}\xi \approx -h_0^*/\Delta\xi_{\mathrm{cor}}$ we arrive at the estimate

$$\Gamma = 1 - G^*\Delta\xi_{\mathrm{cor}}h_0^*\frac{W}{4R_0C_2} = 1 - \frac{G^*\Delta\xi_{\mathrm{cor}}}{4} \tag{29}$$

As in Eq. (26), the furthest right equality corresponds to the particular case where the minimum contact angle is 0. Further, since G^* must be less than unity for the flow to reach the end of the channel and since $\Delta\xi_{\mathrm{cor}}$ is usually $\ll 1$ for the flows of interest here, the effects of gravity on the corner-flow region are generally unimportant. If desired, more complete analytical treatments of the corner-flow region can be developed using approaches previously applied to channels having triangular cross sections [5–7].

7. Analytical solution for large aspect ratios

When the aspect ratio is large, the meniscus remains attached to the top corners of the channel over most of

the wetted length, as suggested by the numerical solutions in Fig. 6. Under these conditions, the meniscus curvature increases and the liquid pressure decreases with distance owing to changes in the contact angle, but there is very little reduction in the saturation of a high aspect ratio channel. Even for a contact angle of 0, the maximum possible reduction in saturation is readily found to be only $\pi/(8A)$ or about 8% for an aspect ratio of $A = 5$. Thus, for large A, it is permissible to analytically integrate Eq. (12) assuming that the saturation, s, and the friction coefficient, β, remain uniform along the flow path to obtain

$$p_\ell^*(\xi) = p_\ell^*(0) - G^*\xi - Q^*\frac{\bar{\beta}}{\bar{s}}\left(\xi - \frac{\xi^2}{2}\right) \tag{30}$$

where the overbars on $\bar{s}$ and $\bar{\beta}$ indicate suitably chosen average values, approaching 1 and 12, respectively, in the limit of large A.

The maximum sustainable heat flux is defined here as the largest value of Q^* for which the fluid penetrates the full length of the channel to $\xi = 1$. In the limit of high aspect ratio this condition corresponds to a fully depressed meniscus at the far end of the channel, or equivalently, $p_\ell^* = -1$ at $\xi = 1$. A greater heat flux would necessitate a saturation jump from near unity to a small value of order $1/A$, since only the bottom corners contain liquid on the downstream side of the jump. Further, as seen earlier in Fig. 6 for $A = 10$, the fluid penetration beyond the jump is very small when A is large. Thus, setting $p_\ell^*(1) = -1$ in Eq. (30), the maximum sustainable heat flux is estimated as

$$Q_{\max}^* = 2\frac{\bar{s}}{\bar{\beta}}(1 + p_0^* - G^*) \leqslant \frac{1}{6}(1 - G^*) \tag{31}$$

The inequality in Eq. (31) applies to the optimal case where the inlet meniscus is flat ($p_0^* \equiv p_\ell^*(0) = 0$) and the aspect ratio is sufficiently large that $\bar{s} \to 1$ and $\bar{\beta} \to 12$. As expected, the maximum flux goes to 0 when $G^* \to 1 + p_0^* = \Delta p^*$. In this limiting case the maximum available capillary pressure, $\Delta p^* \Delta p_0$, is equal to the gravitational pressure head, $\rho g_x L$, leaving no excess capillary pressure to drive the flow.

An improved approximation of the maximum heat flux can be obtained by matching the meniscus deformation solution of the present section with the corner-flow solution of the preceding section. Under conditions of maximum sustainable heat flux, the meniscus now becomes fully depressed at the match point between regions, $\xi = \xi_M$. Accordingly, $p^*(\xi_M) = -1$ and we can rewrite Eq. (30) as

$$Q_{\max}^* = \frac{\bar{s}}{\bar{\beta}}\frac{(1 + p_0^* - G^*\xi_M)}{\left(\xi_M\left(1 - \frac{\xi_M}{2}\right)\right)} = \frac{\bar{s}}{\bar{\beta}}\frac{(1 + p_0^* - G^*\xi_M)}{\frac{1}{2}(1 - \Delta\xi_{cor}^2)} \tag{32}$$

where $\Delta\xi_{cor} \equiv 1 - \xi_M$ is the fractional extent of the corner-flow region relative to the overall wetted length of the channel, here taken as unity for convenience of notation. Another expression for the maximum heat flux is obtained from Eqs. (26) and (27).

$$Q_{\max}^* = \frac{Q_{\max,cor}^*}{\Delta\xi_{cor}^2} = \widehat{Q}_{\max}^* \frac{C_1 C_2 R_0}{D\beta\Delta\xi_{cor}^2} = \frac{3.8 \times 10^{-4}}{2A\Delta\xi_{cor}^2} \tag{33}$$

Here, we have used the fact that the maximum sustainable flux in the corner region is proportional to $1/\Delta\xi^2$, as explained in earlier discussion of Eq. (27). Also, in the last equality of Eq. (33) the constants are evaluated for a minimum contact angle of 0 in which case $D/R_0 = D/(W/2) = 2A$. Equating these two alternative expressions for the maximum heat flux, Eqs. (32) and (33), yields the following expression for $\Delta\xi_{cor}$.

$$\Delta\xi_{cor} = \sqrt{\frac{1}{1 + 2\Theta}}, \quad \text{where } \Theta = 2A\frac{\bar{s}}{\bar{\beta}}\frac{(1 + p_0^* - G^*\xi_M)}{3.8 \times 10^{-4}} \tag{34}$$

Since $\Delta\xi_{cor}$ is usually small and $G^* < 1$, it is usually sufficient to set $\xi_M \approx 1$ in Eq. (34) to obtain an initial approximation that can be iteratively improved.

The solid lines in Fig. 9 show the relative extent of the corner-flow region, $\Delta\xi_{cor}/\xi_D$, computed form Eq. (34) for $G^* = 0$. This expression is valid for any choice of the overall wetted length to the dryout point, ξ_D, not just for the special case of unit length, $\xi_D = 1$, considered in the derivation of Eq. (34). This generality holds because the maximum sustainable heat fluxes are inversely proportional to the square of the wetted length in both regions of the flow. To demonstrate this generality, the symbols shown on the plot were taken from the numerical solutions shown in Fig. 6 for various aspect ratios; all of these had $\xi_D < 1$. For a relatively flat entry meniscus, say $-0.5 \leqslant p_0^* \leqslant 0$, the relative extent of the corner-flow region is less than 0.1 for all aspect ratios greater than unity. Thus, under these circumstances, the meniscus deformation region comprises 90% of the overall wetted length. Even for a relatively deeply bowed meniscus having $p_0^* = -0.9$ the meniscus deformation region comprises more than 80% of the wetted length for all aspect ratios greater than unity. Thus, it is only when the entry meniscus is almost fully

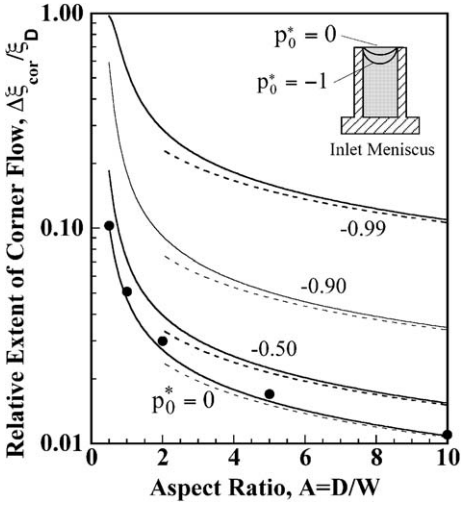

Fig. 9. Relative extent of corner flow region versus aspect ratio for various choices of the normalized inlet pressure, p_0^*, with $G^* = 0$, $\alpha_{min} = 0°$. Solid lines are from Eq. (34). Dotted lines are from simplified form of Eq. (34) for large aspect ratio. Symbols are from numerical calculations in Fig. 6.

depressed that the corner flow becomes a dominant consideration.

Fig. 9 illustrates good agreement between the analytical approximation of Eq. (34) and the numerical results shown by symbols. An even simpler approximation shown by dotted lines in Fig. 9 is applicable for relatively large aspect ratios, $A > 2$ or 3, where we can make the substitutions $\bar{s} \approx 1$ and $\bar{\beta} \approx 12$ in Eq. (34). It is certainly possible to construct intermediate approximations having accuracy between the two levels of approximation shown in Fig. 9. However, as explained further in the next section and in Appendix A, it is not difficult to compute the quantities $\bar{s}$ and $\bar{\beta}$ appearing in Eq. (34).

Once the location of the match point $\xi_M = 1 - \Delta\xi_{cor}$ is known from Eq. (34), the maximum heat flux can be calculated from either Eq. (32) or Eq. (33). However, given that the meniscus deformation region usually accounts for the great majority of the heat removal, one can obtain quite a good approximation by simply adding the maximum sustainable flux for the corner flow predicted by Eq. (26) to that predicted by Eq. (31).

$$Q^*_{max} \approx 2\frac{\bar{s}}{\bar{\beta}}(1 + p^*_0 - G^*) + Q^*_{max,cor} \tag{35}$$

This ensures that we recover the correct corner-flow limit when the meniscus is fully depressed at the channel inlet and, hence, $p^*_0 = -1$. This simple approximation also provides very good agreement with numerical calculations of the maximum flux, as demonstrated in the next section.

A matching between flow regions, similar to that in Eqs. (32)–(34), can also be used to account for the increased cooling capacity associated with a gravity-aided flow traversing a portion of the "dead zone", as explained earlier in the context of Fig. 7. The breadth of this gravity-aided zone, $\xi_D - \xi_G$, is related to Q^*, G^*, and the saturation and friction coefficient, s_G and β_G, at the match point, ξ_G, through the following rearrangement of Eq. (13a)

$$Q^*_{max} = -\frac{s_G}{\beta_G}\frac{G^*}{(1 - \xi_G)} > 0 \tag{36}$$

Here again we have for convenience set $\xi_D = 1$, corresponding to incipient dryout at the end of the channel. As before, a second expression for the heat flux is obtained by evaluating Eq. (30) between the inlet and the match point, ξ_G. This is identical to the first equality in Eq. (32), except that ξ_M is replaced by ξ_G. Since the heat flux is assumed uniform along the channel, Eqs. (32) and (36) can be equated to obtain a quadratic equation for the match point location, ξ_G.

$$\frac{1}{2}\xi^2_G + \Omega\xi_G - \Omega = 0, \quad \text{where } \Omega = -\frac{1 + p^*_0}{G^*} > 0 \tag{37}$$

This simplified quadratic assumes that the values of s and β at the match point, s_G and β_G, are the same as the average values over the upstream flow, $\bar{s}$ and $\bar{\beta}$. The following solution to Eq. (37)

$$\xi_G = -\Omega + \sqrt{\Omega^2 + 2\Omega} \tag{38}$$

is simply substituted back into Eq. (32) or (36) to compute the maximum sustainable heat flux. Comparisons of the preceding analytical approximations with numerical results are presented in the next section.

8. Dryout heat fluxes

The maximum sustainable heat flux, as limited by the viscous flow considerations modeled here, is commonly referred to as the capillary limit. This limiting flux, q''_{max}, is the maximum value for which the wetting fluid penetrates the full length of the channel. The corresponding normalized flux, Q^*_{max}, can be determined by computing a sequence of solutions for gradually increasing Q^* until reaching the value for which the saturation is barely zero at the end of the channel. Further increases in Q^* result in a dry section near the end that is no longer cooled by evaporation. In a device having a uniform flux over its full length, the energy flux into the dry portion would cause a sharp temperature rise and a shifting of some of the heat load by conduction toward the cooler end, causing further fluid recession. Although the present model does not include this redistribution of energy, it can still be used to predict the onset of dryout, the quantity of greatest practical interest.

The dimensional heat flux, q''_{max}, corresponding to the dryout limit can be readily computed by substituting the numerically calculated value of Q^*_{max} into the following rearrangement of the defining equation, Eq. (7):

$$q''_{max} = Q^*_{max} D\rho H_{fg}\frac{W^3}{W_b L^2}\frac{\Delta p_0}{\mu} \tag{39}$$

Alternatively, one can also calculate the maximum penetration length, L_{max}, of fluid drawn into a heated channel by capillary suction.

$$L_{max} = \left[Q^*_{max} D\rho H_{fg}\frac{W^3_0}{W_b q''}\frac{\Delta p_0}{\mu}\right]^{1/2} \tag{40}$$

This wetted length has been frequently used as an experimental indication of channel performance and as a means of checking the validity of mathematical models, though mainly for channels of triangular cross section [2–4,6,7].

Eq. (40) also serves as the basis of a non-iterative approach for calculating Q^*_{max}. For any initial guess, Q^*_{trial}, we compute the normalized fluid penetration, ξ_{trial}, as the dryout point where the saturation goes to 0. Since penetration lengths are inversely proportional to the square root of the applied flux, in accordance with Eq. (40), it follows that a normalized maximum flux of $Q^*_{max} = Q^*_{trial}\xi^2_{trial}$ will permit fluid penetration to precisely the endpoint of the channel where $\xi = 1$. However, multiple iterations are still required when $G^* = \rho g_x L/\Delta p_0$ is nonzero, since this parameter is dependent on the wetted length of the channel.

Fig. 10 compares numerically computed values of the maximum heat flux (symbols) with the analytical predic-

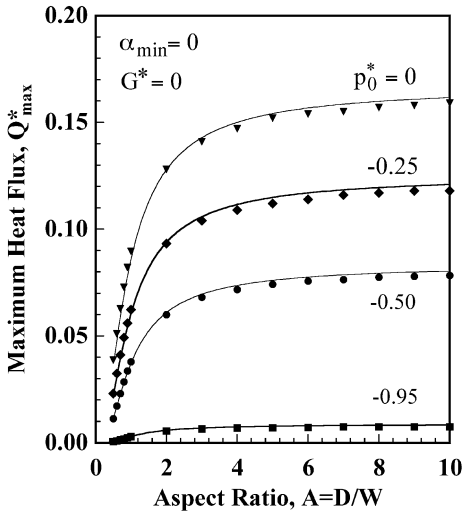

Fig. 10. Comparison of analytical (lines) and numerical (symbols) predictions of maximum sustainable heat flux for various choices of the normalized inlet pressure, p_0^*, with $G^* = 0$, $\alpha_{\min} = 0°$.

tions of Eq. (35). The most striking feature of the plot is the large benefit of increasing aspect ratio, though there is not much additional increase in $Q^*_{\max}$ for $A > 5$. In addition to the order of magnitude increases of $Q^*_{\max}$ apparent in the plot, there is an additional linear increase of the actual heat flux, $Q_{\max}$, due to the appearance of the channel depth, D, in Eq. (39).

The strong influence of the inlet pressure or, equivalently, the curvature of the meniscus at the inlet is also clearly apparent in Fig. 10. For an aspect ratio of $A = 0.5$, the maximum flux for a channel having a liquid-full inlet with a flat meniscus ($p_0^* = 0$) is about 0.04 as compared with the value of 0.00038 predicted by Eq. (26) for a fully bowed inlet meniscus ($p_0^* = -1$). This hundredfold difference is ignored in models that assume the meniscus to be fully bowed at the inlet, as done in many previous analyses of flow in grooves having triangular cross sections. As the channel aspect ratio increases, the influence of the inlet curvature becomes less pronounced but still exceeds one order of magnitude.

The agreement between numerical and analytical results in Fig. 10 is generally quite good. Here, the analytical results are computed from Eq. (35) using average values of the saturation and friction coefficient, $\bar{s}$ and $\bar{\beta}$, based on an average contact angle, $\bar{\alpha} = \omega\alpha_0 + (1-\omega)\alpha_e$, that weights the inlet value, α_0, twice as heavily (i.e. $\omega = 2/3$) as the end value, α_e, in recognition that the flow rate decreases linearly with distance owing to fluid evaporation. Under conditions of maximum flux $\alpha_e = \alpha_{\min}$ and the corresponding inlet contact angle is given by $\cos\alpha_0 = -p_0^* \cos\alpha_{\min}$. After calculating the weighted average of α, the corresponding value of the mean saturation $\bar{s}$ is computed from Eqs. (A1) and (A2) and $\bar{\beta}$ follows from (A4)–(A7). This sequence of calculations is performed with no required root finding or iterations. The agreement between analytical and numerical results in Fig. 10 is good enough to suggest that further refinement of our analytical model would not yield substantial improvement.

Fig. 11 shows that the normalized value of the maximum sustainable heat flux, $Q^*_{\max}$, is nearly insensitive to the value of the minimum contact angle over the range from $\alpha_{\min} = 0$ and 40°. However, this insensitivity is mainly an indication of appropriate scaling, since Q^* is normalized by a pressure differential that depends upon the minimum wetting angle, $\Delta p_0 = 2\sigma\cos\alpha_0/W$. Thus, in accordance with Eq. (39), the actual value of the maximum heat flux, $q''_{\max}$, increases linearly with $\cos\alpha_0$. The normalized maximum heat flux is expected to increase somewhat with increasing contact angle because the reduced downward bowing of the meniscus increases the fluid depth and reduces the friction. However, this influence appears to be sufficiently moderate that it is almost negligible, and it is certainly negligible in the limit of large aspect ratio.

The agreement between numerical and analytical results in Fig. 11 is excellent for small aspect ratios. However, for aspect ratios greater than about $A = 2$ the numerical results for $\alpha_{\min} = 40°$ become increasingly inaccurate owing to numerical oscillations occurring as the saturation jump moves back and forth across the grid lines nearest the jump. Higher aspect ratios increase the magnitude of the pressure jump, while larger contact angles appear to amplify the numerical noise, which is further compounded by the severely singular nature of the corner-flow structures adjacent to the jump. As a result, the numerical solutions suggest that the normalized heat flux for $\alpha_{\min} = 40°$ is a few percent less than that for $\alpha_{\min} = 0°$ for aspect ratios greater than about $A = 4$. We know that this cannot be the case in the limit of very large aspects ratios where the analytical result becomes increasingly more reliable than the numerical result. For that reason we have not included the numerical results beyond the range shown. The main conclusion to be drawn is that variations in the minimum

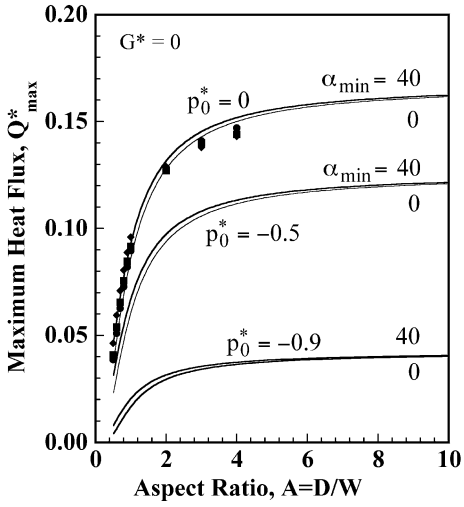

Fig. 11. Comparison of maximum sustainable heat fluxes for two choices of minimum contact angle, $\alpha_{\min}$, with $G^* = 0$. Normalization of $Q^*_{\max}$ by $\cos\alpha_{\min}$ has largely removed dependence on $\alpha_{\min}$. Lines and symbols are analytical and numerical predictions, respectively.

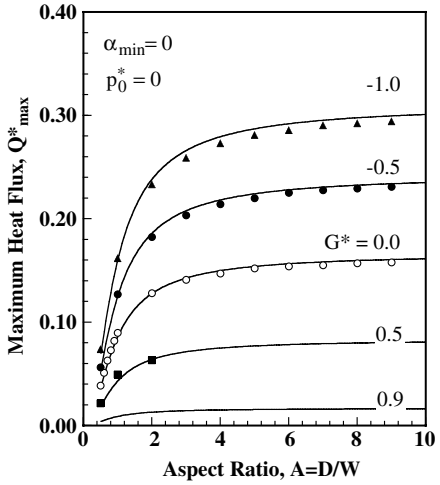

Fig. 12. Variation of maximum sustainable heat flux with normalized gravitational force, G^*, for $p_0^* = 0$ and $\alpha_{min} = 0°$. Lines and symbols are analytical and numerical predictions, respectively.

contact angle are very well accounted for by the scaling of Q^*. The considered range of contact angles $0° \leqslant \alpha_{min} \leqslant 40°$ is probably representative of those likely to be used in evaporative cooling applications, particularly since there can be no corner flow ahead of the jump for $\alpha_{min} \geqslant 45°$ as discussed earlier.

The influence of gravitational forces is illustrated in Fig. 12. As expected, the maximum sustainable heat flux is reduced when $G^* > 0$ because the gravitational force opposes the flow. Conversely, Q^*_{max} is increased when $G^* < 0$ and the gravitational force aids the flow. The solid lines represent analytical predictions based on Eqs. (36)–(38) which include the gravity-aided flow traversing a portion of the "dead zone" when $G^* < 0$. When $G^* \geqslant 0$, these equations become equivalent to Eq. (35) used in constructing Figs. 10 and 11.

The agreement between analytical and numerical results in Fig. 12 is good for $G^* \leqslant 0$. This is partly because the magnitude of the saturation jump is reduced by an aiding gravitational force. However, as noted earlier, the numerical results for $G^* \geqslant 0$ sometimes become noisy, particularly when aspect ratios (and hence saturation jumps) are large, and this is aggravated by increasing large positive values of G^*. Fortunately, we have very high confidence in the analytical results when the aspect ratio is large, which is precisely where the numerical calculations become suspect. In addition, the numerical results appear quite reliable at the lower aspect ratios where the analytical model is in greatest need of verification. Thus, the two solutions methods complement one another and provide confidence in the analytical model over the full range of conditions.

9. Summary

Analytical and numerical solutions have been used to investigate steady evaporating flows in open rectangular microchannels. The flow structure was found to generally consist of two principal regions, an entry region where the meniscus remains attached to the top corners of the channel followed by a corner-flow region where the meniscus recedes into the bottom corners of the channel. The transition between these regions generally involves a jump-like change in the fluid depth as the meniscus detaches from the top corners and attaches to the channel floor. In cases where gravity aids the flow, a portion of this transitional jump is replaced by a third flow region in which the meniscus is attached to the channel side walls as it gradually descends toward the floor.

In addition to numerical modeling, analytical solutions were derived for each of the preceding flow regions. Exact analytical solutions were used to verify the accuracy of the numerical model in dealing with the jump-like transition in the middle of the flow and the severe singularities of fluid pressure and velocity at the leading edge where the fluid saturation approaches 0. Also, approximate analytical models of the three regions were joined together into a relatively simple composite model that predicts maximum sustainable heat fluxes within a few percent of the numerical results.

The evaporative cooling capability of rectangular channels was presented in terms of a maximum sustainable heat flux, Q^*_{max}, scaled in a manner intended to eliminate first order dependence on channel dimensions, flow parameters, and fluid properties. Despite this scaling, Q^*_{max} increases several fold as the channel aspect ratio (depth/width) increases from 0.5 to 5. Q^*_{max} is also extremely sensitive to the fluid configuration at the inlet, decreasing by about three orders of magnitude as the inlet meniscus varies from a flat orientation with essentially no curvature at the inlet to a deeply bowed meniscus having the maximum inlet curvature. In the latter case of a fully bowed inlet meniscus, an abrupt reduction in fluid depth occurs just beyond the inlet, leaving the downstream flow confined to the corners of the channel. Conversely, the much flatter inlet meniscus of a liquid-full channel provides the maximum axial variation in the capillary pressure and by far the greatest flow capacity.

These observations regarding the benefits of a large channel depth and a flat entry meniscus must, however, be weighed against two offsetting considerations. Although an increased channel depth provides more axial fluid flow, it also increases the length of the conduction path and hence increases the temperature difference between the channel base where heat is applied and the meniscus contact region where evaporation is intended to occur. If this temperature difference should become excessive, boiling will occur at the channel base, hindering performance. Fortunately, moderate temperature differences are acceptable because the increased pressure inside small bubbles helps to elevate the vaporization temperature [1,17]. Similarly, a flatter entry meniscus, and hence a larger contact angle, increases the liquid pressure at the inlet, thereby providing a larger pressure difference to drive the axial capillary flow. Conversely, previous analyses of the meniscus contact region [18,19] indicate that the heat flow to an evaporating meniscus is maximized at zero contact angle. Thus, optimal

choices of design parameters and operating conditions will require a comprehensive model that includes all of these physical processes. Although the goal of the present study was to investigate fundamental aspects of capillary flow in rectangular channels, the resulting analytical relationships may ultimately be combined with compact models of the other processes to arrive at convenient and comprehensive tools for design of evaporative cooling device.

Acknowledgements

This work was supported by the Sandia Engineering Sciences Research Foundation. Sandia is a multiprogram laboratory operated by Sandia Corporation, a Lockheed Martin Company, for the United States Department of Energy's National Nuclear Security Administration under contract DE-AC04-94AL85000.

Appendix A

For a fully spanning meniscus ($h_c > 0$), the rectangular channel shown in Fig. 2 contains a liquid volume fraction, or saturation, given by

$$s = \frac{W}{2D}\left[\frac{2h}{W} - \frac{1}{\Lambda} - \frac{\pi - 2(\alpha+\theta) - \sin[2(\alpha+\theta)]}{8\cos^2\theta\cos^2(\alpha+\theta)}\right] \tag{A1}$$

where

$$\Lambda = \frac{W}{h-h_c} = \frac{2\cos\alpha}{1-\sin\alpha} \quad \text{and} \quad \tan\theta = \frac{2}{\Lambda} \tag{A2}$$

For corner flows ($h_c = 0$), Eq. (A1) takes a slightly different form in which $\theta = \pi/4$:

$$s = \frac{h^2}{WD}\left[1 - \frac{\pi - 2(\alpha+\theta) - \sin[2(\alpha+\theta)]}{4\cos^2\theta\cos^2(\alpha+\theta)}\right] \tag{A3}$$

Thus, the constant C_1 appearing in Eqs. (18), (20), (23) and (26) is identified as the square bracketed term in Eq. (A3).

The friction coefficient β appearing in Eq. (3) is evaluated using the analytical expressions derived in [16]. In that study, the velocity distribution was calculated for a wide range of channel geometries and fluid depths by numerically solving the two-dimensional Poisson equation relating the axial pressure gradient, dp/dz, to the viscous forces in the cross sectional plane of the channel. The mean fluid speed, u, was then computed by averaging the local fluid speed over the region of the channel containing liquid. This speed was then normalized to obtain a non-dimensional speed, U^*, that is similar to the dimensionless mean speed, u^*, defined in Eq. (11). They differ in that U^* is normalized by the local pressure gradient, dp/dz, whereas u^* is normalized by the maximum capillary pressure Δp_0 divided by the channel length. To avoid confusion, it is helpful to define a friction coefficient, β, that is the reciprocal of U^*, for use in the present momentum equation, Eq. (3).

$$\frac{1}{\beta} \equiv U^* = \frac{U\mu}{W^2(dp/dz)} \tag{A4}$$

Generalized analytical expressions for U^* are derived in [16] by blending of asymptotic expressions that apply in limits of high and low aspect ratios and limits of small and large contact angles. The blend is implemented using the following expression that applies to any pair of asymptotes, U_1^* and U_2^*:

$$U^* = \left[\frac{(U_1^* U_2^*)^m}{(U_1^*)^m + (U_2^*)^m}\right]^{1/m} \tag{A5}$$

This composite function reduces to U_1^* in the limit when $U_1^* \ll U_2^*$ and, conversely, reduces to U_2^* when $U_2^* \ll U_1^*$. The parameter m controls the shape of the transition between asymptotes. This expression is first applied to corner flows ($h_c = 0$ in Fig. 2) using asymptotic expressions that apply in the limits of small and large contact angles to obtain

$$U_c^* = \left[\frac{U_{c,0}^m}{1 + (U_{c,0}^*)^m[7(\Lambda-2)^2 + b(\Lambda-2)^k]^m}\right]^{1/m} \tag{A6}$$

Here $U_{c,0}^* = 0.0027$, is the mean speed of a corner flow having a contact angle of $\alpha = 0$, and the function $\Lambda(\alpha)$ is defined by Eq. (A2). Eq. (A6) agrees with numerical calculations within a relative error of 2% with the parameters m, b, and k set to 1.88, 150, and 0.87. The linear term involving b and k is included to improve the fit without affecting the asymptotes of $U_1^* = U_{c,0}^*$ and $U_2^* = 1/[7(\Lambda - 2)^2]$ that apply in the limits of small ($\alpha \to 0$, $(\Lambda - 2) \to 0$) and large ($\alpha \to \pi/2$, $\Lambda \to \infty$) contact angle.

To obtain a comprehensive expression describing the mean speed for all contact angles and aspect ratios the asymptotes in Eq. (A5) are chosen as

$$U_1^* = \frac{1}{12} \quad \text{and} \quad U_2^* = \left[\left(\frac{1}{a\lambda + 3\lambda^3}\right)^n + (U_c^*)^n\right]^{1/n} \tag{A7}$$

where $\lambda = W/h_c$ and h_c is the fluid depth at the channel center. The left asymptote $U_1^* = 1/12$ applies in the limit where the fluid depth greatly exceeds the width ($\lambda \to 0$); here, the fluid friction is equivalent to that between infinite parallel plates. The right asymptote U_2^* approaches one of two alternative limits as the liquid depth becomes very shallow at the center ($\lambda \to \infty$). The corner flow solution is recovered for any finite U_c^*; otherwise the mean speed decreases as $1/3\lambda^2$ as appropriate for a contact angle of 90°. When Eqs. (A7) are substituted into Eq. (A5) with the parameters taken as $m = 1.31$, $n = 0.82$, and $a = 2.6$, the mean speed is approximated within a maximum relative error of 10% for contact angles in the range $0° \leqslant \alpha \leqslant 60°$.

References

[1] A. Faghri, Heat Pipe Science and Technology, Taylor and Francis Publishers, New York, NY, 1995.

[2] G.R. Stroes, T.J. Rohloff, I. Catton, An experimental study of the capillary forces in rectangular vs. triangular channels, in: Proceedings of the 28th National Heat Transfer Conference, August 9–12, San Diego, HTD-vol. 200, 1992, pp. 1–7.

[3] G.R. Stroes, I. Catton, An experimental study of the capillary performance of triangular versus sinusoidal channels, ASME J. Heat Transfer 119 (1997) 851–853.
[4] A. Sivaraman, S. De, S. Dasgupta, Experimental and theoretical study of axial dryout point for evaporation from V-shaped micro-grooves, Int. J. Heat Mass Transfer 45 (2002) 1535–1543.
[5] X. Xu, V.P. Carey, Film evaporation from a micro-grooved surface—an approximate heat transfer model and its comparison with experimental data, J. Thermophys. 4 (4) (1990) 512–520.
[6] I. Catton, G.R. Stroes, A semi-analytical model to predict the capillary limit of heated inclined triangular capillary grooves, ASME J. Heat Transfer 124 (2002) 162–168.
[7] J.M. Ha, G.P. Peterson, The interline heat transfer of evaporating thin films along a micro grooved surface, ASME J. Heat Transfer 118 (1996) 747–755.
[8] Y.P. Peles, S. Haber, A steady one dimensional model for boiling two phase flow in a triangular microchannel, Int. J. Multiphase Flow 26 (2000) 1095–1115.
[9] P.C. Stephan, C.A. Busse, Analysis of heat transfer coefficient of grooved heat pipe evaporator walls, Int. J. Heat Mass Transfer 35 (2) (1992) 383–391.
[10] L. Lin, A. Faghri, Heat transfer in micro region of a rotating miniature heat pipe, Int. J. Heat Mass Transfer 42 (1999) 1363–1369.
[11] V. Satre, M.C. Zaghdoudi, M. Lallemand, Effect of interfacial phenomena on evaporative heat transfer in micro heat pipes, Int. J. Therm. Sci. 39 (2002) 498–504.
[12] P.S. Ayyaswamy, I. Catton, D.K. Edwards, Capillary flow in triangular grooves, ASME J. Appl. Mech. (1974) 332–336.
[13] J.-S. Suh, R. Greif, C.P. Grigoropoulos, Friction in micro-channel flows of a liquid and vapor in trapezoidal and sinusoidal grooves, Int. J. Heat Mass Transfer 44 (2001) 3103–3109.
[14] T.C. Ransohoff, C.J. Radke, Laminar flow of a wetting liquid along the corners of predominantly gas-occupied noncircular pore, J. Colloid Interf. Sci. 121 (2) (1987) 392–400.
[15] S.K. Thomas, R.C. Lykins, K.L. Yerkes, Fully developed laminar flow in trapezoidal grooves with shear stress at the liquid–vapor interface, Int. J. Heat Mass Transfer 44 (2001) 3397–3412.
[16] S.W. Tchikanda, R.H. Nilson, S.K. Griffiths, Modeling of pressure and shear driven flows in open rectangular microchannels, Int. J. Heat Mass Transfer 47 (2004) 527–538.
[17] P.C. Wayner, Intermolecular forces in phase-change heat transfer: 1998 Kern award review, AIChE J. 45 (10) (1999) 2055–2068.
[18] S.J.S. Morris, Contact angles for evaporating liquids predicted and compared with existing experiments, J. Fluid Mech. 432 (2001) 1–30.
[19] S.J.S. Morris, The evaporating meniscus in a channel, J. Fluid Mech. 494 (2003) 297–317.
[20] E.W. Becker, W. Ehrfeld, P. Hagmann, A. Maner, D. Munchmeyer, Fabrication of microstructures with high aspect ratios and great structural heights by synchrotron radiation lithography, galvano-forming and plastic moulding (LIGA Process), Microelectron. Eng. 4 (1986) 35–56.
[21] W. Ehrfeld, A. Schmidt, Recent developments in deep X-ray lithography, J. Vac. Sci. Technol. B 16 (6) (1998) 3526–3534.
[22] M. Van Dyke, Perturbation Methods in Fluid Mechanics, Academic Press, New York, NY, 1964.